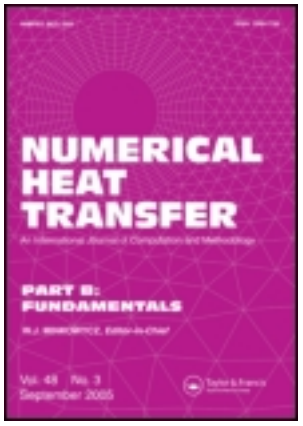

Numerical Heat Transfer, Part B: Fundamentals

Publication details, including instructions for authors and subscription information:
http://www.tandfonline.com/loi/unhb20

Benchmark Solution for a Three-Dimensional Mixed-Convection Flow, Part 1: Reference Solutions

Xavier Nicolas [a], Marc Medale [b], Stéphane Glockner [c] & Stéphane Gounand [d]

[a] Université Paris-Est, Laboratoire Modélisation et Simulation Multi Echelle, MSME UMR 8208 CNRS, Marne-la-Vallée, France

[b] Aix-Marseille Université IUSTI, UMR 6595 CNRS, Technopôle de Château-Gombert, Marseille, France

[c] Université de Bordeaux, IPB ENSCBP, CNRS UMR 5295, Institut I2M, Pessac, France

[d] CEA-Saclay, DEN, DM2S, SFME, LTMF, Gif-sur-Yvette, France

Available online: 28 Oct 2011

To cite this article: Xavier Nicolas, Marc Medale, Stéphane Glockner & Stéphane Gounand (2011): Benchmark Solution for a Three-Dimensional Mixed-Convection Flow, Part 1: Reference Solutions, Numerical Heat Transfer, Part B: Fundamentals, 60:5, 325-345

To link to this article: http://dx.doi.org/10.1080/10407790.2011.616758

Numerical Heat Transfer, Part B, 60: 325–345, 2011

ISSN: 1040-7790 print/1521-0626 online
DOI: 10.1080/10407790.2011.616758

Taylor & Francis
Taylor & Francis Group

BENCHMARK SOLUTION FOR A THREE-DIMENSIONAL MIXED-CONVECTION FLOW, PART 1: REFERENCE SOLUTIONS

Xavier Nicolas[1], Marc Medale[2], Stéphane Glockner[3], and Stéphane Gounand[4]

[1]*Université Paris-Est, Laboratoire Modélisation et Simulation Multi Echelle, MSME UMR 8208 CNRS, Marne-la-Vallée, France*

[2]*Aix-Marseille Université IUSTI, UMR 6595 CNRS, Technopôle de Château-Gombert, Marseille, France*

[3]*Université de Bordeaux, IPB ENSCBP, CNRS UMR 5295, Institut I2M, Pessac, France*

[4]*CEA-Saclay, DEN, DM2S, SFME, LTMF, Gif-sur-Yvette, France*

A solution to a benchmark problem for a three-dimensional mixed-convection flow in a horizontal rectangular channel heated from below and cooled from above (Poiseuille-Rayleigh-Bénard flow) is proposed. This flow is a steady thermoconvective longitudinal roll flow in a large-aspect-ratio channel at moderate Reynolds and Rayleigh numbers ($Re = 50$, $Ra = 5{,}000$) and Prandtl number $Pr = 0.7$. The model is based on the Navier-Stokes equations with Boussinesq approximation. We propose reference solutions resulting from computations on large grids, Richardson extrapolation (RE), and cubic spline interpolations. The solutions obtained with one finite-difference, one finite-volume, and two finite-element codes are in good agreement, and reference values for the flow and thermal fields and for the heat and momentum fluxes are given with four to five significant digits.

1. CONTEXT AND OBJECTIVES

Mixed-convection flows in channels of rectangular cross section are encountered in many industrial applications: thermal and chemical reactors, chimneys, solar collectors, thermal insulation of buildings, heat exchangers, etc. More specifically, the

Received 18 March 2011; accepted 6 August 2011.

Xavier Nicolas acknowledges Shihe Xin, from CETHIL, UMR 5008 CNRS/Insa-Lyon, France, for providing the finite-difference code, FD1, that was developed by him when he was at LIMSI, CNRS, UPR 3251, Orsay, France. The authors acknowledge Donna Calhoun for proofreading of the article and providing many useful suggestions. This work was supported by CNRS, which provided substantial computational resources on its NEC-SX5 vectorial supercomputer and on its IBM SP4 and SP6 parallel supercomputers at IDRIS, Orsay, France, under project numbers 06-1823 and 07-1823. Stéphane Glockner thanks the Aquitaine Regional Council for the financial support dedicated to a 256-processor cluster investment, located at I2M Institute.

Address correspondence to Xavier Nicolas, Université Paris-Est Marne la Vallée, Laboratoire MSME UMR 8208 CNRS, Bâtiment Lavoisier, 5 bd Descartes, 77454 Marne La Vallée Cedex 2, France. E-mail: xavier.nicolas@univ-paris-est.fr

NOMENCLATURE

A, A_e	streamwise and adiabatic entrance aspect ratios of the channel, ($=L/H$, L_e/H)
B	transversal aspect ratio of the channel, ($=l/H$)
d_f	relative distance between the finest grid and extrapolated solutions, $[=(f^{fg}-f^{ex})/\lvert f^{fg}\rvert]$
E_c	kinetic energy
FD, FV	finite differences, finite volumes
FE	finite elements
g	gravitational acceleration, m/s^2
h, h_i	cell size or space step of a grid
H	channel height, m
I_{buo}	integral of the buoyancy term on the half computational domain
$\vec{k}$	upward vertical unit vector
l	channel width, m
L, L_e	channel and adiabatic entrance lengths, m
$N_{x/y/z}$	cell number in the x, y, or z directions
Nu	Nusselt number
p	dimensionless deviation of pressure from hydrostatic pressure
Pr	Prandtl number, ($=\nu/\alpha$)
PRB	Poiseuille-Rayleigh-Bénard
r	regularity order of a problem
Ra	Rayleigh number, $[=g\beta(T_h-T_c)H^3/(\nu\alpha)]$
Re	Reynolds number, ($=U_{mean}H/\nu$)
RE	Richardson extrapolation
S	boundary surface of the channel
t	dimensionless time
T	temperature, K
T_c, T_h	temperatures of the top cold and bottom hot walls of the channel, K
T_m	dimensionless mean temperature of the whole computational domain
u, v, w	dimensionless streamwise, spanwise, and vertical velocity components
u_{Pois}	dimensionless Poiseuille profile in the rectangular channel (function of x and y)
U_{mean}	mean velocity of the flow in a rectangular channel, m/s
$\vec{v}$	dimensionless velocity vector, $[=(u, v, w)]$
x, y, z	dimensionless streamwise, spanwise, and vertical coordinates
α	thermal diffusivity, m^2/s
α	observed convergence order from RE or "extrapolation coefficient" of RE
α°	consistency order or formal convergence order of the numerical method
β	thermal expansion coefficient, K^{-1}
ΔP_{io}	mean pressure difference between inlet and outlet
Δt	dimensionless time step
θ	reduced temperature, $[=(T-T_c)/(T_h-T_c)]$
ν	kinematic viscosity, m^2/s
ρ	mass per volume unit, kg/m^3

Subscripts

b	bottom
exact	exact solution of the problem
f	front
h	discrete solution of the problem on a grid of space step h
i	inlet
marg	uncertainty margin on a value
o	outlet
prec	precision of a reference value ($f_{prec}=f_{marg}/f_{ref}$)
ref	reference value
s	symmetry
t	top
tot	total

Superscripts

ex	extrapolated value by RE
fg	solution on the finest grid
$\sim$	approximated value

Poiseuille-Rayleigh-Bénard (PRB) configuration (i.e., mixed-convection flows in horizontal rectangular channels heated from below) is representative of rectangular chemical vapor deposition (CVD) reactors and of air flows in the cooling of printed electronic circuit boards, among others [1–3]. PRB flows are also studied in association with mass transfer in the case of double-diffusive mixed-convection flows, with

or without Soret effect [4, 5]. However, to the authors' best knowledge, three-dimensional benchmark numerical solutions of mixed-convection flows do not exist in the literature. In numerous numerical studies of PRB flows, for instance, numerical codes are validated only by comparisons with experimental data, particularly those of Chiu and Rosenberger [6] and Ouazzani et al. [7], in which laser Doppler anemometry measurements of local velocities are given. However, it is well known that precise agreement between experimental and numerical results is hard to obtain because the thermal and dynamical initial and boundary conditions are not perfectly controlled experimentally and are very hard to accurately reproduce numerically [8]. That is why we propose the present benchmark solution.

This benchmark exercise was proposed in the framework of the French Heat Transfer Society (SFT) by several laboratories involved in the numerical analysis of thermoconvective flows in closed cavities and open channels. A call for contributions was first published in 2006 [9]. Initially, two configurations of PRB flows, covering two different flow ranges, were chosen. The first one concerned the present steady longitudinal roll flow in a large-aspect-ratio channel at Reynolds number $\mathrm{Re} = 50$, Rayleigh number $\mathrm{Ra} = 5{,}000$, and Prandtl number $\mathrm{Pr} = 0.7$. The second one concerned a fully established space and time periodic transverse roll flow in a small-aspect-ratio channel at small Reynolds number $\mathrm{Re} = 0.1$, $\mathrm{Ra} = 2500$, and $\mathrm{Pr} = 7$. In this article, only the solution of the first test case is presented.

The computation of 3-D unsteady mixed-convection flows in channels often requires computational domains of long and/or wide aspect ratios, with fine space and time discretizations. Therefore, efficient numerical methods are needed to solve the conservation equations. The interest of this first test case is that its computational cost is quite reasonable and it is accessible with limited computational facilities. It is indeed steady and, the computational domain being extended up to the fully established zone, a homogeneous Neumann boundary condition at the outflow accommodates the problem solution. It is therefore much easier to compute than the second test case, in which a steady state is never established since unsteady thermoconvective rolls are permanently transported by the flow.

Thus the aim of the present article is to provide a 3-D numerical benchmark solution for mixed-convection flows that can be used, for instance, to validate 3-D numerical codes for the computation of thermoconvective instabilities in channels. More precisely, local, surface-averaged, and volume-averaged quantities, concerning the temperature, velocity, and pressure fields and their derivatives, are computed. For all these quantities, reference values with their uncertainty margins are given in tables.

In the present work, we solve the first benchmark problem using four different computational fluid dynamics (CFD) research codes and three discretization methods: finite-difference (FD), finite-volume (FV), and finite-element (FE) methods. Two of the solvers (the FD and FV ones) are, theoretically, of second order in space, while both the others (the FE solvers) are of third order. All contributors have mobilized a significant amount of computational resources to achieve reliable spatial convergence. In particular, approximate solutions have been obtained on successively refined grids so that Richardson extrapolation (RE) could be used to extend the results. This technique enables one to improve the accuracy of the discrete solutions when used in the asymptotic range of the numerical methods [10–13]. In the present

study, RE was mainly performed for increasing the accuracy of the second-order solvers since an improvement by one unit of the space convergence order is theoretically achievable, which would allow one to reach the same space order as the FE methods.

However, in the present test case, difficulties in the use of RE have appeared due to the mixed thermal boundary conditions on the channel bottom and top plates. Indeed, to try to reproduce the operating conditions of the PRB experiments by Pabiou et al. [14] without introducing too many parameters (a regularizing function, for instance), we chose to impose adiabatic Neumann conditions near the inlet and isothermal Dirichlet conditions downstream. This generates a continuous temperature field but a discontinuous temperature gradient at the boundary condition junction. The consequences of this singularity are discussed thoroughly in the second part of this article [15]. In this more technical and theoretical second part, it is shown that RE can still be used, but with precautions, and that reference solutions for the present benchmark problem can be indeed given with four to five significant digits.

The outline of the present article is as follows. The geometry, the governing equations, the boundary conditions, and the flow parameters of the simulated test case are described in Section 2. The solvers of the different contributors are presented in Section 3, and references are given for more details. In Section 4, the general principle of RE is first recalled and the methodology used to define the reference solutions is described. The reference solutions are presented and analyzed in Section 5. In Section 5.1, reference solutions are given for the volume averages of kinetic energy and temperature over the whole domain and for the pressure difference between the inlet and the outlet of the channel. In Section 5.2, streamwise and spanwise profiles of the velocity components, temperature, and wall Nusselt number are presented and reference values for selected extrema on these profiles are given. In Section 5.3, reference values of the heat and momentum fluxes through the channel boundaries are presented. Finally, a brief conclusion is given in section Section 6.

2. TEST CASE DESCRIPTION

The proposed benchmark is a PRB flow, made of 10 steady longitudinal thermoconvective rolls, in the horizontal rectangular channel drawn in Figure 1.

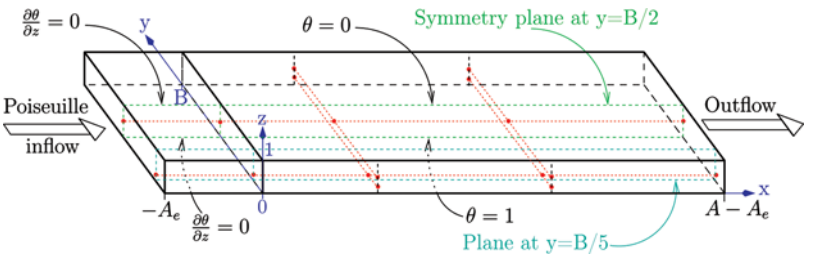

Figure 1. Geometry and thermal boundary conditions on the top and bottom walls (the vertical lateral walls are adiabatic). The dotted lines are the lines along which θ, *u*, *v*, and *w* profiles and their extrema are calculated (color figure available online).

A Poiseuille flow is imposed at the channel entrance and the incoming fluid is cold, at temperature T_c. After an entrance zone over which a zero heat flux is imposed on the four walls, the top horizontal wall is maintained at the cold temperature T_c and the bottom wall is maintained at a higher temperature T_h. The vertical lateral walls are adiabatic. A and B are the streamwise and spanwise aspect ratios of the computational domain, and A_e is the streamwise entrance aspect ratio (see Figure 1). The working fluid is Newtonian and the flow is governed by the 3-D incompressible Navier-Stokes equations under the Boussinesq assumption. Using the channel height H, the mean flow velocity U_{mean}, ρU_{mean}^2, and H/U_{mean} as reference quantities for lengths, velocities, pressure, and time, respectively, and using the reduced temperature $\theta = (T - T_c)/(T_h - T_c)$, the governing equations take the following dimensionless form:

$$\begin{cases} \nabla \cdot \vec{v} & = 0 \\ \frac{\partial \vec{v}}{\partial t} + (\vec{v} \cdot \nabla)\vec{v} & = -\nabla p + \frac{1}{\text{Re}} \nabla^2 \vec{v} + \frac{\text{Ra}}{\text{Pr Re}^2} \theta \vec{k} \\ \frac{\partial \theta}{\partial t} + \vec{v} \cdot \nabla \theta & = \frac{1}{\text{Pr Re}} \nabla^2 \theta \end{cases} \tag{1}$$

where x, y, z, t, $\vec{v} = (u, v, w)$, and p are the dimensionless streamwise, spanwise, and vertical coordinates, time, velocity vector, and pressure, $\vec{k}$ is the upward unit vector, Pr is Prandtl number ($= \nu/\alpha$), Re is Reynolds number ($= U_{\text{mean}} H/\nu$), and Ra is Rayleigh number [$= g\beta(T_h - T_c)H^3/(\nu\alpha)$]. The boundary and initial conditions for u, v, w, and θ are as follows:

At $z = 0$, $\vec{v} = \vec{0}$ and there is a Neumann thermal boundary condition, $\partial\theta/\partial z = 0$, for $x \in [-A_e, 0[$ next to a Dirichlet condition, $\theta = 1$, for $x \in [0, A - A_e]$.

At $z = 1$, $\vec{v} = \vec{0}$ and there is also a Neumann thermal boundary condition, $\partial\theta/\partial z = 0$, for $x \in [-A_e, 0[$ next to a Dirichlet condition, $\theta = 0$, for $x \in [0, A - A_e]$.

At $y = 0$ and B, $\vec{v} = \vec{0}$ and $\partial\theta/\partial y = 0$.

At $x = -A_e$, $u = u_{Pois}(y, z)$, $v = w = 0$, and $\theta = 0$, where $u_{Pois}(y, z)$ is given either directly by an approximate solution of the Poisson equation $\left(\partial^2 u_{\text{Pois}}/\partial y^2\right) + \left(\partial^2 u_{\text{Pois}}/\partial z^2\right) = \text{Re}(\partial p/\partial x)$, with no-slip boundary conditions at $y = 0$ and B and at $z = 0$ and 1, or by the analytical solution of this equation computed in [16] and given in the Appendix.

At $x = A - A_e$, an outflow nonreflective boundary condition is imposed. The choice of this boundary condition was left free in [9]. Note, however, that the standard Neumann or Orlanski boundary conditions are appropriate for this test case, since the flow is dominated by convection.

At $t = 0, \forall\, x \in [-A_e, A - A_e]$, $u = u_{Pois}(y, z)$, $v = w = 0$, and $\theta = 0$.

The present test case is defined by $\text{Re} = 50$, $\text{Ra} = 5{,}000$, $\text{Pr} = 0.7$, $A = 50$, $B = 10$, and $A_e = 2$. The resulting flow pattern is the 10 longitudinal roll steady flow presented in Figure 2. It is obtained by starting from the initial conditions given above and develops after a transient stage which will not be discussed here. It is symmetrical with respect to the median longitudinal vertical plane and can therefore be computed for $y \in [0, B/2]$.

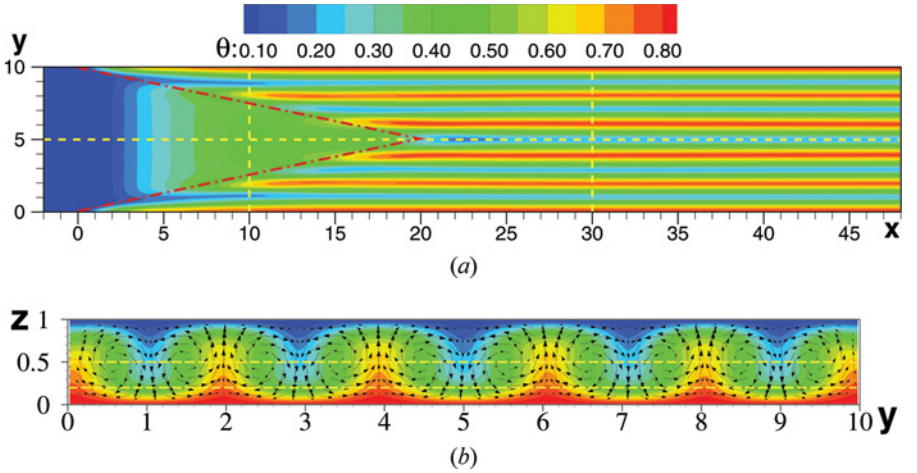

Figure 2. Temperature fields θ in the horizontal mid-plane and temperature field and velocity vector field in the transverse plane at $x = 30$ in the longitudinal roll flow of the present test case. The dashed lines are some of the lines along which θ, u, v, and w profiles and their extrema are calculated. The dash-dotted lines border the forced-convection triangular zone at the entrance of the heated plate, in which no thermoconvective rolls are present (color figure available online).

3. CONTRIBUTORS AND SOLVER DESCRIPTION

Below, we present the solvers of the four contributors, and references are given for more details. The numerical parameters for each of the four schemes are given in Table 1. In the table, we also indicate whether the symmetry with respect to the median longitudinal vertical plane was used, the mesh sizes in each space direction, $N_x \times N_y \times N_z$, the time-step value Δt, an estimation of the computational time (wall time) and the consistency orders in space[1], α°, of each space discretization method for each primitive variable. Note that, when symmetry is used, N_y is the node number on the width $B/2$ of the computational domain. Furthermore, N_i ($i = x, y, z$) is the node number in the direction i for the FV and FE methods and the number of computational points of scalar quantities (temperature and pressure) for the FD method. Thus, whatever the mesh used, the beginning of the bottom heated plate at $x = 0$ is located on a node for the FE and FV methods and at mid-distance between two temperature computational points for the FD method.

3.1. Second-Order Finite-Difference Vectorized Code: FD1

The test case solution "FD1" is computed using a FD method, optimized for vectorial computers. The time discretization scheme is a second-order scheme combining a second-order backward difference formula for the time derivative term, an explicit Adams-Bashforth scheme for the convective term, and an implicit treatment of the diffusive term. The equations are discretized in space on uniform, Cartesian, and staggered grids using centered differences for the diffusive terms and a central scheme for the convective terms. However, with the two finest meshes used in this

[1]the consistency order in space is the formal convergence order that is the leading order of the space discretization truncation error

Table 1. Numerical parameters used by the different contributors

Contributor	$N_x \times N_y \times N_z$ [symmetry]	Δt	Wall time [computer type (organism/lab)]	Consistency orders α°
MSME, FD1	$400 \times 134 \times 40$	0.01	36 min on 1 processor	2 for θ, u, v, w; 2 for p
	$600 \times 200 \times 60$	0.01	2 h 20 on 1 processor	
	$800 \times 268 \times 80$	0.002	25 h on 1 processor	
	$1{,}200 \times 400 \times 120$	0.002	100 h on 1 processor	
	[no]		[NEC SX5 (IDRIS)]	
IUSTI, FE2	$601 \times 121 \times 41$	0.01	19 min on 60 cores	3 for θ, u, v, w; 2 for p
	$901 \times 181 \times 61$	0.01	1 h 40 on 150 cores	
	$1{,}351 \times 271 \times 91$	0.005	43 h 15 on 225 cores	
	[yes]		[IBM SP6 (IDRIS)]	
I2M Institute, FV3	$601 \times 161 \times 41$	0.1	8 h on 152 cores	2 for θ, u, v, w; 2 for p
	$901 \times 241 \times 61$	0.1	12 h on 152 cores	
	$1{,}351 \times 361 \times 91$	0.1	56 h on 152 cores	
	[yes]		[ALTIX ICE 8200 (I2 M Inst.)]	
CEA, FE4	$601 \times 121 \times 49$	0.5	200 h on 8 cores	3 for θ, u, v, w; 2 for p
	$751 \times 151 \times 61$	0.5	400 h on 8 cores	
	$801 \times 161 \times 65$	0.5	450 h on 8 cores	
	$1{,}001 \times 201 \times 81$	0.5	1,600 h on 8 cores	
	[yes]		[PC 8 cores (CEA)]	

study (see Table 1), to avoid numerical scheme instabilities and save CPU time, the solution is computed first with a second-order upwind scheme and $\Delta t = 0.01$. Then, starting from this converged steady solution as initial condition, a new solution is computed with the central scheme and $\Delta t = 0.002$. The time integration and the velocity–pressure coupling are computed by the projection method based on Goda's algorithm [17]. The Helmholtz equations for the temperature field and the components of the predicted velocity field are solved using an incremental factorization method of ADI type which preserves a second-order time accuracy. The Poisson equation for the pressure increment is solved by a factorization method which consists of the partial diagonalizing of the monodimensional Laplace operators in the transverse directions y and z. The linear systems resulting from these two factorization methods are all tridiagonal and are solved by the TDMA algorithm. An Orlanski-type boundary condition is used at the outflow boundary. Steady-state solutions are obtained by integrating long enough in time. The stopping criterion is reached when the maximum of the velocity divergence saturates at values below 5×10^{-12}. Since this solver is highly vectorizable, the code is very efficient on vectorial supercomputers: for instance, it runs at 12.5 gigaflops on average on the NEC-SX8 computer at IDRIS (the CNRS supercomputing center at Orsay, France), when the peak power of this computer is 16 gigaflops. A detailed description of this code and of its validations and performances can be found in Benzaoui et al. [8].

3.2. Third-Order Finite-Element Parallelized Code: FE2

The numerical model "FE2" is based on a segregated approach to build up separate integral forms associated with the set of coupled governing equations (1).

The fluid flow problem is kept in primitive-variable formulation and solved using an unconditionally stable projection algorithm [18]. As in most projection-type algorithms, the incompressibility constraint is enforced in the FE2 code through a pressure-correction field computed from a pressure Poisson equation. The latter is obtained by taking the divergence of the momentum equation in Eqs. (1) and Neumann boundary conditions. Nonhomogeneous Neumann boundary conditions have been implemented for the pressure Poisson equation in a form derived from [19, 20]:

$$\frac{\partial p}{\partial \vec{n}} = \left(-\frac{\partial \vec{v}}{\partial t} - \vec{v}\nabla\vec{v} - \frac{1}{\mathrm{Re}}\nabla \times (\nabla \times \vec{v}) + \frac{\mathrm{Ra}}{\mathrm{PrRe}^2}\theta\vec{k} \right) \cdot \vec{n} \tag{2}$$

The mechanical stress and heat flux outlet boundary conditions arising at $x = A$ for the momentum and energy equations have been treated with a formulation inspired from [21] and adapted to the present framework combining a segregated approach for the mixed-convection problem together with a projection algorithm.

The spatial discretization of the three separate integral forms, associated with temperature, velocity, and pressure unknowns, follows the standard FE method, using triquadratic hexahedral FE for the velocity and temperature fields and trilinear approximation for the pressure field. The nonlinear algebraic system resulting from the discretization of the momentum equation is solved using a Newton-Raphson procedure, despite only partial convergence being required for solving this nonlinear system during the transient solution in the segregated procedure. The time integration is performed with a second-order backward difference formula scheme (BDF2) [18]. At each time step, the three algebraic systems corresponding to the momentum, incompressible projection, and energy conservation are solved with an iterative solver (bi-conjugate gradient stabilized, pre-conditioned with the additive Schwartz method) provided in the PETSc toolkit [22]. This implementation enables us to efficiently run high-performance, massively parallel computers (IBM SP4 and SP6 at IDRIS). Finally, the computational domain is discretized with three meshes uniformly spaced in the x, y, and z directions and whose node numbers are given in Table 1, e.g., the finest mesh consists of $675 \times 135 \times 45$ triquadratic hexahedra FE, built on $1{,}351 \times 271 \times 91$ nodes. The stopping criterion is reached when the L^2 norm of the time derivative terms of velocity components and temperature, divided by the total number of degrees of freedom, is smaller than 10^{-12}.

3.3. Second-Order Finite-Volume Parallelized Code: FV3

The test case solution "FV3" is computed using the FV code Thétis developed at I2 M Institute. Time discretization of the Navier-Stokes and energy equations is implicit. A first-order Euler scheme is used, with an implicit treatment of all the terms of the equations (after linearization of the nonlinear convective term of the Navier-Stokes equations and after uncoupling with the energy equation). The incompressibility constraint that couples the velocity and the pressure is solved using a pressure-correction scheme [23]. It consists of splitting the Navier-Stokes system into two stages, a velocity-prediction stage and a pressure-correction stage. The spatial discretization is based on the FV method on a velocity–pressure staggered grid.

Pressure and temperature unknowns are located at the cell vertices, whereas velocity components are face-centered. A centered scheme of order 2 is used for the nonlinear convective terms and stress terms of the Navier-Stokes equations, as well as for the pressure-correction step and the diffusive term of the energy equation. The convective term of the latter equation is discretized with the Quick scheme to avoid numerical instabilities [24]. A Neumann boundary condition is set on the outlet boundary for velocity and temperature. The code is parallelized in a distributed way [25] and runs efficiently on hundreds of processors using the parallel solver library Hypre [26]. Among the different solvers and preconditioners available in this library, the most efficient for this problem are a GMRES solver for the prediction step and the energy equation with a point Jacobi preconditioner. For the correction step, a BiCGStab solver with a multigrid preconditioner is used. Three meshes were used. The first one begins with 601 cells in direction x to avoid small oscillations observed in the temperature field with coarser meshes. Simulations are stopped when both the stationary criterion (L^∞ norm of the absolute difference of temperature and velocity between two time iterations) of 10^{-10} is reached and the L^2 norm of the divergence is below 10^{-10}. An SGI Altix 8200 cluster was used composed of 32 eight-core dual Intel Xeon processor blades.

3.4. Third-Order Finite-Element Stationary Parallelized Code: FE4

The numerical model "FE4" spatially discretizes Eqs. (1) in stationary form (without the temporal derivative term) using an LBB-stable [27] FE method. No upwinding of the convective term is used. To find the solution of the discrete nonlinear stationary problem, we used a defect-correction solver [28]. A certain linearization of the equations and additional regularization terms give an inexact tangent matrix. This tangent matrix is then approximately factorized as in the algebraic projection method [29]. This leads to segregation of the linear systems to be solved for each scalar incremental unknown (3 velocities, 1 pressure, 1 temperature).

The mesh is regular and consists of hexahedral elements, triquadratic (Q_2) for the velocity and temperature unknowns and linear discontinuous (P_1^{nc}) for the pressure. Thus, the formal spatial discretization order of the method is 3 for the velocity and temperature unknowns and 2 for the pressure unknown. The total number of degrees of freedom is 16 million for the coarsest mesh and 73.3 million for the finest one. The standard natural boundary condition on momentum for the discretization used [27] is $\mu\,\partial u_n/\partial n - P = 0$. A boundary term in $-P_{\text{last}}$ (the last pressure estimation) is discretized and added to the right-hand side of the boundary condition so that we get the desired $\mu\,\partial u_n/\partial n = 0$ when convergence is reached. The inexact tangent matrix is obtained from the following contributions: exact tangent matrix for the diffusion, pressure gradient, and velocity divergence terms, fixed point linearization for the convective terms, and a regularizing pseudo-time-like mass term on the velocity and temperature. The linear systems are solved with BiCGSTAB preconditioned by an ILU(0) incomplete factorization [30] for the velocity and temperature unknowns and FCG(1) preconditioned by algebraic multigrid for the pressure unknown. We used the algebraic multigrid method of Notay [31] in sequential mode. To speed up convergence toward the final steady state, a four-point acceleration method is used. For all computational results, it was checked that the L^∞ norm of the vector of the final incremental unknowns was less than 10^{-10} and that the L^∞

norm of the final residual vector was less than 10^{-11}. The numerical model was implemented in Cast3m [32], a freely available FE code developed at CEA (French Atomic Energy Commission). The model was run on standard PC servers running Linux with up to 8 cores and 64 GB RAM. The most CPU-intensive part of the model is the solution of the pressure linear systems.

4. COMPUTATION METHOD OF REFERENCE VALUES

4.1. Principle of Richardson Extrapolation

When the approximate solutions of a continuous initial- and boundary-value problem are computed by discretization methods such as FD, FV, or FE methods, RE can be used to improve the accuracy of the discrete solutions. Indeed, provided that some assumptions are satisfied (see below), it is possible to get an order of accuracy of at least $O(h^{p+1})$ when the convergence order of the numerical method is $O(h^p)$, where h is the mesh size. This technique then allows one to compute extrapolated primitive variables at any point of the computational domain as well as solution functionals such as differentiated or integrated quantities (heat and momentum fluxes, volume- or surface-averaged quantities, etc.). A concise and elegant presentation of RE to estimate *a posteriori* discretization errors in computational simulations can be found in [10]. More details and deeper discussions on the theory are given in [11–13]. Here we present the RE principle to compute extrapolated values. The aim is to briefly review its general principle, but for a completely rigorous presentation one should refer to the second part of this article [15].

RE first consists of computing the numerical solutions f_{h_i} $(1 \leq i \leq N)$ of the discretized boundary-value problem on N different nested uniform grids of size h_i, with h_1 the coarsest grid and h_N the finest one. If the exact solution of the continuous problem, f_{exact}, is sufficiently smooth to justify the use of Taylor expansion (at least up to the discretization order), then it can be written in the form

$$f_{h_i} = f_{\text{exact}} + C_\alpha h_i^\alpha + O(h_i^{\alpha+1}) \tag{3}$$

where C_α is a coefficient which is dependent on α but independent of h_i. Then, the leading order α of the truncation error due to discretization, the coefficient C_α, and the exact solution f_{exact} can be approximated from the discrete solutions, if the mesh spacings h_i used in the extrapolation are small enough so that the discrete solutions f_{h_i} are located in the asymptotic convergence region: that is, the leading-order term $C_\alpha h_i^\alpha$ of the truncation error must dominate the total discretization error $f_{\text{exact}} - f_{h_i}$. Thus, using three grids ($N = 3$), such as $h_1/h_2 = h_2/h_3$, the approximations $\tilde{\alpha}$, $\widetilde{C}_\alpha$, and $\tilde{f}^{\text{ex}}$ of α, C_α, and f_{exact} in Eq. (3) are given by [12, 13]:

$$\begin{aligned} \tilde{\alpha} &= \frac{\ln[(f_{h_1} - f_{h_2})/(f_{h_2} - f_{h_3})]}{\ln(h_1/h_2)} \\ \widetilde{C}_\alpha &= \frac{f_{h_2} - f_{h_3}}{h_2^{\tilde{\alpha}} - h_3^{\tilde{\alpha}}} \\ \tilde{f}^{ex} &= f_{h_3} - \widetilde{C}_\alpha h_3^{\tilde{\alpha}} \end{aligned} \tag{4}$$

and, using four grids ($N=4$) such as $h_1/h_2 = h_3/h_4$, they are given by

$$\tilde{\alpha} = \frac{\ln[(f_{h_1} - f_{h_3})/(f_{h_2} - f_{h_4})]}{\ln(h_1/h_2)}$$
$$\widetilde{C}_\alpha = \frac{f_{h_3} - f_{h_4}}{h_3^{\tilde{\alpha}} - h_4^{\tilde{\alpha}}} \tag{5}$$
$$\tilde{f}^{ex} = f_{h_4} - \widetilde{C}_\alpha h_4^{\tilde{\alpha}}$$

with $\widetilde{C}_\alpha = C_\alpha + O(h_{N-1})$ and $\tilde{f}^{\text{ex}} = f_{\text{exact}} + O(h_N^{\tilde{\alpha}+1})$. As a consequence, the approximation $\tilde{f}^{\text{ex}}$ of the asymptotic solution f_{exact} will be better if h_N is small and $\tilde{\alpha}$ is large.

The RE technique can therefore be used to increase the accuracy of discrete solutions if the problem is smooth enough. Since the present benchmark problem does not satisfy this assumption, the aim of the second part of this article [15] is precisely to show that RE can still be used when a temperature gradient discontinuity is present in the boundary conditions of the problem. In this case, however, numerous precautions and several verifications must be done in order to guarantee the RE validity. For each extrapolated quantity, it must be checked that the associated extrapolation coefficient, $\tilde{\alpha}$, varies between the order of the regularity of the problem (equal to 1 in the present benchmark problem; see [15]) and the convergence order of the numerical method used (equal to 2 or 3 according to the contributors of the present article). Of course, for all the quantities presented in the present article, this requirement has been checked when a value extrapolated by RE is used to compute a reference value.

4.2. Criteria Used to Define the Reference Values

All the reference solutions presented in the present article have been computed from the solutions obtained by the four contributors with their laboratory codes using the fine grids presented in Table 1 and the stringent convergence criteria described in section 3. Since these codes have second- and third-order space accuracies, RE has mainly been used to increase the accuracy of the lower-order methods in order to homogenize the accuracy of the four solutions. It has indeed been shown in [15] that, in our specific case (including the problem at hand and the particular methods and meshes used), RE is relevant to increase the accuracy of most of the quantities computed with the FD1 and FV3 second-order methods, even if a singularity in the temperature gradient is present in the boundary conditions. Nevertheless, in this case, one must carefully check the validity of RE for each extrapolated quantity. On the other hand, it has also been shown in [15] that in our specific case RE could not be used most of the time with the FE4 method and sometimes with the FE2 method.

As a consequence, the reference solutions proposed in the present article have been constructed by averaging the extrapolated values obtained from RE of the FD1 and FV3 solutions and the extrapolated values or the values on the finest grid of the FE2 and FE4 methods, depending on whether RE succeeds or not. More precisely, for each quantity proposed in this article, the reference value, f_{ref}, is equal to the arithmetic average of the extreme values of the FD1, FE2, FV3, and FE4 extrapolated values, except if the validity of RE is not satisfied by the FE solutions.

In this case, each value of the FE method for which RE fails is replaced by its counterpart on the finest grid. The uncertainty margin, f_{marg}, of the reference solution is simply defined as the half-difference between the two extreme values of the four contributors. These definitions have the advantage to be very simple and to give a quick criterion to evaluate the dispersion of the best solutions of the four contributors. We have also defined the precision of the reference solution determination, f_{prec}: it is equal to the ratio of the uncertainty margin to the reference value. The values of f_{ref}, f_{marg}, and f_{prec} computed for various integral, local, or derivative quantities characteristic of the velocity, pressure, and thermal fields of the present PRB flow are given in the result tables of section 5.

5. PRESENTATION AND ANALYSIS OF THE REFERENCE VALUES

5.1. Reference Values for Integral Quantities

The reference values of integral quantities are given first. These integrals are twice the mean kinetic energy, $2E_c$, on the whole domain of volume D, the mean pressure difference, ΔP_{io}, between inlet and outlet, and the mean temperature, T_m, on the whole domain, which are defined by

$$2E_c = \frac{1}{D}\int\int\int_D (u^2 + v^2 + w^2)\,dx\,dy\,dz \tag{6}$$

$$\Delta P_{io} = \frac{1}{S_i}\int\int_{S_i} P\,dy\,dz - \frac{1}{S_o}\int\int_{S_o} P\,dy\,dz \tag{7}$$

$$T_m = \frac{1}{D}\int\int\int_D \theta\,dx\,dy\,dz \tag{8}$$

They have been computed using either the middle-point rule for the FD1 and FV3 solutions or $3 \times 3 \times 3$ Gauss integration scheme for the FE2 and FE4 solutions. The advantage of these integrals is that they depend only on the primitive variables: no differentiation and no interpolation are needed to compute their values on each grid. Thus, the accuracy of these quantities depend only on the convergence orders of the numerical methods.

The values of $f = (2E_c, \Delta P_{io}, T_m)$ on the finest grid (denoted f^{fg}) and extrapolated by RE (denoted f^{ex}) are given in Table 2 with the associated convergence order $\tilde{\alpha}_f$. It can be shown that RE fails only for the FE4 $2E_c$ and ΔP_{io} values because $\tilde{\alpha}_{E_c}$ and $\tilde{\alpha}_{\Delta P_{io}}$ do not vary between 1 (the order of the regularity of the problem) and 3 (the accuracy order of the the FE4 method). Reference solutions can nevertheless be constructed using the FE4 $2E_c$ and ΔP_{io} values on the finest grid by following the method proposed in section 4.2. The reference values of the three integral quantities are given in Table 2 with a precision of the order of 10^{-5}, with five common figures among the four extrapolated solutions for $2E_c$ and ΔP_{io} and four common figures for T_m. The relevance of RE on the accuracy of these results is discussed thoroughly in [15].

Table 2. Left columns: finest grid (f^{fg}) and extrapolated (f^{ex}) values of the integral functions $f = 2E_c$, ΔP_{io}, and T_m, and truncation error leading order, $\tilde{\alpha}_f$, from their RE. FE4 column: the symbol ° indicates an erroneous value due to the extrapolation failure (thus the FE4 finest-grid value replaces the FE4 extrapolated value in the reference value determination). Right column: reference solutions with their tolerance margin and the precision of their determination

	FD1	FE2	FV3	FE4	References $f_{\text{ref}} \pm f_{\text{marg}}$ $f_{\text{prec}} = \frac{f_{\text{marg}}}{f_{\text{ref}}}$
$2E_c^{fg}$	1.292479	1.292452	1.292355	1.292461	1.292453
$2E_c^{\text{ex}}$	1.292446	1.292452	1.292455	1.292467°	±0.000008
$\tilde{\alpha}_{E_c}$	2.22	2.92	2.00	−1.92°	6.19×10^{-6}
ΔP_{io}^{fg}	14.41210	14.40784	14.40235	14.40694	14.40670
$\Delta P_{io}^{\text{ex}}$	14.40647	14.40649	14.40678	14.40658°	±0.00024
$\tilde{\alpha}_{\Delta P_{io}}$	2.03	1.99	2.00	0.83°	1.67×10^{-5}
T_m^{fg}	0.448490	0.448625	0.448725	0.448659	0.448604
T_m^{ex}	0.448594	0.448604	0.448606	0.448613	±0.000010
$\tilde{\alpha}_{T_m}$	1.19	1.18	1.02	1.18	2.23×10^{-5}

5.2. Reference Values for Temperature, Velocity, and Nusselt Number Local Extrema

5.2.1. Space profiles of the thermal and dynamical fields. In the following, we denote by Nu_t and Nu_b the local Nusselt numbers on the top and bottom walls, respectively. They are defined by

$$\text{Nu}_{t,b}(x,y) = -\frac{H(\partial T/\partial Z)_{Z=H,Z=0}}{T_h - T_c} = -\left(\frac{\partial \theta}{\partial z}\right)_{z=1,z=0} \tag{9}$$

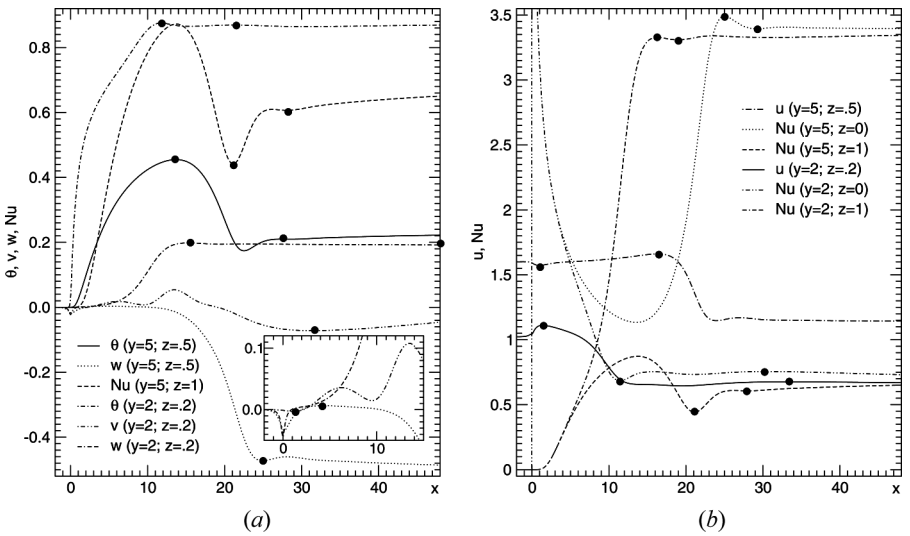

Figure 3. Longitudinal profiles of θ, u, v, and w along the lines at $(y, z) = (2, 0.2)$ and $(5, 0.5)$ and longitudinal profiles of Nu_t and Nu_b along the lines at $y = 2$ and $y = 5$. These profiles are the same for the four contributors. The filled circles indicate the local extrema whose values and coordinates are given in Tables 3 and 4.

In Figure 3, the longitudinal profiles of the primitive variables θ, u, v, and w are plotted along the lines $(y, z) = (2, 0.2)$ and $(5, 0.5)$, and the profiles of Nu_t and Nu_b are plotted along the lines $y = 2$ and $y = 5$. The transverse profiles of θ, u, v, and w are drawn in Figure 4 along the four lines at $x = 10$ and 30 and at $z = 0.2$ and 0.5. The transverse profiles of Nu_t and Nu_b are drawn in Figure 5 along the lines at $x = 10$ and $x = 30$. Only the first half of these transverse profiles is shown, because the flow is symmetrical with respect to the median vertical plane ($y = 5$). The transverse profiles at $x = 10$ are located in the entrance region, more precisely at mid-length of the forced-convection triangular zone, where only two longitudinal rolls are present along each vertical wall (see Figure 2*a*). On the other hand, the

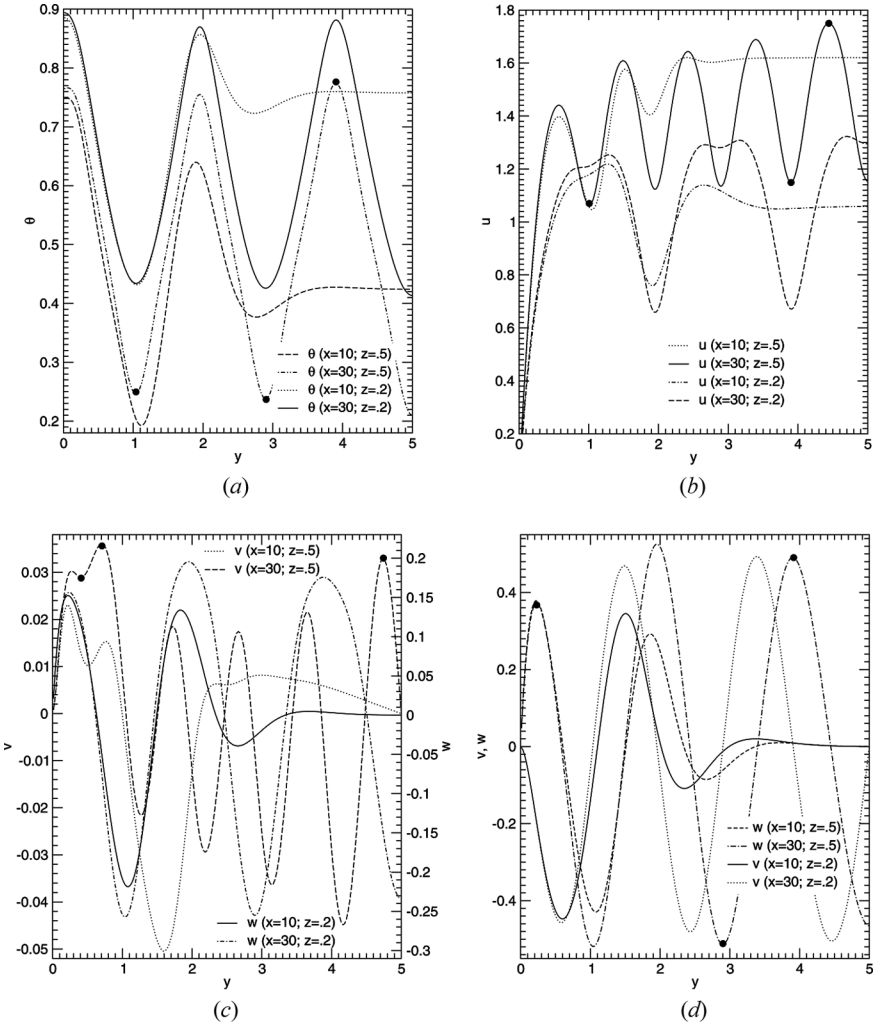

Figure 4. Spanwise profiles of the primitive variables θ, u, v, and w obtained by the four contributors along the lines at $(x, z) = (10, 0.2)$, (10, 0.5), (30, 0.2) and (30, 0.5). The filled circles indicate the local extrema whose values and coordinates are given in Table 3.

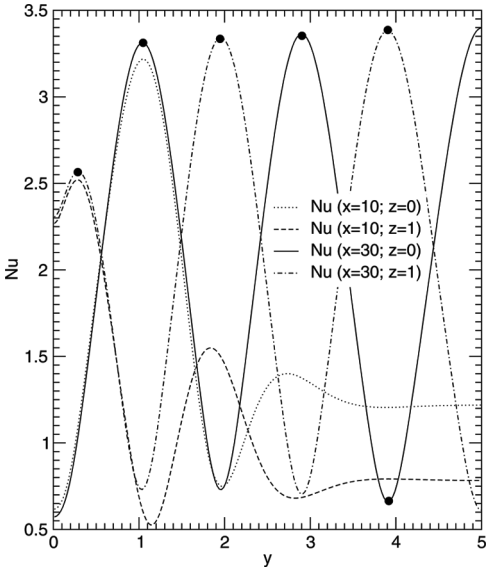

Figure 5. Transverse profiles of the Nusselt numbers Nu_t and Nu_b obtained by the four contributors along the lines at $x = 10$ and $x = 30$. The filled circles indicate the local extrema whose values and coordinates are given in Table 4.

transverse profiles at $x = 30$ are sinusoidal profiles because they are located where 10 well-developed longitudinal rolls are present.

All these profiles are computed from the FD1 solution on the finest mesh. The same profiles are obtained with the other numerical methods (FE2, FV3, FE4) if the comparisons are done at the same scales as those of Figures 3, 4, and 5. Note that the extrapolated profiles cannot be drawn, since the asymptotic convergence region does not span the whole computational domain. In particular, RE diverges at points where the profiles computed on two distinct meshes intersect. Indeed, when $f_{h_i} = f_{h_j}$ for $h_i \neq h_j$, α diverges in Eqs. (4) or (5). This is discussed in detail in [15].

5.2.2. Temperature, velocity, and Nusselt number local extrema. The reference values and the coordinates of 34 local extrema, identified by small filled circles on the profiles of Figures 3–5 along the lines at $(y, z) = (5, 0.5)$ and $(2, 0.2)$ and at $(x, z) = (30, 0.5)$, are given in this section. Only the reference values are given here. They are computed with the method described in section 4.2. However, the method used to compute the values of these extrema on each grid and their extrapolated values requires cubic spline interpolations. This part of the method is described in [15]. The extrapolated values and the values on the finest grid computed by the four contributors for some of these extrema are also given in [15]. Among the 34 chosen extrema, the reference values of the local extrema of the primitive variables, θ, u, v, and w are given in Table 3 with four to five significant figures. The reference values of the Nusselt numbers Nu_t and Nu_b are given in Table 4 with three to four significant figures. The coordinates of these extrema are generally given with three significant figures in the x direction and with four significant figures in the y direction. Note that other extrema and coordinate values are also available in [33].

Table 3. Reference values of the local extrema of $f=(\theta, u, v, w)$ and of their coordinates along the two streamwise lines at $(y, z)=(5, 0.5)$ and $(2, 0.2)$ and the spanwise line at $(x, z)=(30, 0.5)$. The precision on the primitive variables $f_{\text{prec}}=f_{\text{marg}}/f_{\text{ref}}$ is also indicated. Other extrema values at intermediate coordinates y_2 along the line at $(x, z)=(30, 0.5)$ are given in [33]

	$f_{\text{ref}} \pm f_{\text{marg}}$ $x_{\text{ref}} \pm x_{\text{marg}}$ at $(y, z)=(5, 0.5)$	$f_{\text{ref}} \pm f_{\text{marg}}$ $x_{\text{ref}} \pm x_{\text{marg}}$ at $(y, z)=(2, 0.2)$		$f_{\text{ref}} \pm f_{\text{marg}}$ $y_{\text{ref}} \pm y_{\text{marg}}$ at $(x, z)=(30, 0.5)$
θ_1	$(454{,}845 \pm 2) \times 10^{-6}$	$(87{,}525 \pm 4) \times 10^{-5}$	θ_1	$(24{,}716 \pm 3) \times 10^{-5}$
x_1	13.693 ± 0.003	11.742 ± 0.004	y_1	1.0364 ± 0.0004
$\theta_{1\text{prec}}$	4.4×10^{-6}	4.6×10^{-5}	$\theta_{1\text{prec}}$	1.2×10^{-4}
θ_2	$(210{,}055 \pm 7) \times 10^{-6}$	$(869{,}518 \pm 16) \times 10^{-6}$	θ_3	$(77{,}385 \pm 2) \times 10^{-5}$
x_2	27.322 ± 0.010	21.169 ± 0.010	y_3	3.9041 ± 0.0002
$\theta_{2\text{prec}}$	3.3×10^{-5}	1.8×10^{-5}	$\theta_{3\text{prec}}$	2.6×10^{-5}
u_1	$(1{,}572{,}720 \pm 7) \times 10^{-6}$	$(1{,}111{,}322 \pm 4) \times 10^{-6}$	u_1	$(106{,}506 \pm 7) \times 10^{-5}$
x_1	0.945 ± 0.005	1.376 ± 0.004	y_1	1.0086 ± 0.0001
$u_{1\text{prec}}$	4.5×10^{-6}	3.6×10^{-6}	$u_{1\text{prec}}$	6.6×10^{-5}
u_2	$(1{,}660{,}806 \pm 20) \times 10^{-6}$	$(67{,}549 \pm 6) \times 10^{-5}$	u_3	$(174{,}975 \pm 13) \times 10^{-5}$
x_2	16.294 ± 0.005	33.802 ± 0.018	y_3	4.4425 ± 0.0000
$u_{2\text{prec}}$	1.2×10^{-5}	8.9×10^{-5}	$u_{3\text{prec}}$	7.4×10^{-5}
v_1	0.0	$(-14{,}772 \pm 3) \times 10^{-7}$	v_1	$(35{,}904 \pm 12) \times 10^{-6}$
x_1		1.133 ± 0.006	y_1	0.7047 ± 0.0004
$v_{1\text{prec}}$		2.0×10^{-4}	$v_{1\text{prec}}$	3.3×10^{-4}
v_2	0.0	$(-7{,}040 \pm 9) \times 10^{-5}$	v_3	$(32{,}892 \pm 25) \times 10^{-6}$
x_2		31.462 ± 0.008	y_3	4.7391 ± 0.0004
$v_{2\text{prec}}$		1.3×10^{-3}	$v_{3\text{prec}}$	7.6×10^{-4}
w_1	$(32{,}598 \pm 7) \times 10^{-7}$	$(19{,}827 \pm 6) \times 10^{-5}$	w_1	$(37{,}243 \pm 6) \times 10^{-5}$
x_1	4.259 ± 0.007	15.328 ± 0.010	y_1	0.2285 ± 0.0001
$w_{1\text{prec}}$	1.8×10^{-4}	3.0×10^{-4}	$w_{1\text{prec}}$	1.6×10^{-4}
w_2	$(-473{,}007 \pm 19) \times 10^{-6}$	$(19{,}175 \pm 5) \times 10^{-5}$	w_3	$(49{,}041 \pm 7) \times 10^{-5}$
x_2	24.902 ± 0.005	48.0	y_3	3.9028 ± 0.0001
$w_{2\text{prec}}$	4.0×10^{-5}	2.6×10^{-4}	$w_{3\text{prec}}$	1.4×10^{-4}

5.3. Heat and Momentum Fluxes through Channel Faces

Finally, we compare the dimensionless heat flux, Φ_θ, and momentum fluxes, Φ_u, Φ_v, and Φ_w, through the boundary surfaces of the half-channel obtained when the symmetry through the mid-plane at $y=B/2$ is taken into account. The flux definitions are given in Table 5. In this table, S_i, S_o, S_f, S_t, and S_b are respectively the inlet, outlet, front, top, and bottom surfaces of the half-channel, S_s is the symmetry plane at $y=B/2$, and $S_{\text{tot}}=S_i \cup S_o \cup S_f \cup S_s \cup S_t \cup S_b$ is the total surface of the half channel $\Omega/2$. Note that, from the Navier-Stokes equation in (1), the total momentum flux, Φ_w, through S_{tot} is equal to the integral of the buoyancy term, $I_{\text{buo}} = \int_{\Omega/2} \left[-(\text{Ra}/\text{Re}^2\text{Pr})\theta\right] dV$, on the half-computational domain.

The diagonal terms of the momentum flux tensor depend on pressure. Since pressure is defined up to a constant, we decided to fix the value of this constant such

Table 4. Reference values of the local extrema of the Nusselt numbers Nu_t and Nu_b on the top and bottom plates and of their coordinates along the two streamwise lines at $y=5$ and 2 and the spanwise line at $x=30$. The precision on the Nusselt numbers $\mathrm{Nu}_{\mathrm{prec}}=\mathrm{Nu}_{\mathrm{marg}}/\mathrm{Nu}_{\mathrm{ref}}$ is also indicated. Other extrema values at intermediate coordinates y_2 along the line at $x=30$ are given in [33]

	$\mathrm{Nu}_{\mathrm{ref}}\pm\mathrm{Nu}_{\mathrm{marg}}$ $x_{\mathrm{ref}}\pm x_{\mathrm{marg}}$ at $y=5$	$\mathrm{Nu}_{\mathrm{ref}}\pm\mathrm{Nu}_{\mathrm{marg}}$ $x_{\mathrm{ref}}\pm x_{\mathrm{marg}}$ at $y=2$		$\mathrm{Nu}_{\mathrm{ref}}\pm\mathrm{Nu}_{\mathrm{marg}}$ $y_{\mathrm{ref}}\pm y_{\mathrm{marg}}$ at $x=30$
Nu_{t1}	0.44135 ± 0.00016	3.3218 ± 0.0018	Nu_{t1}	2.5628 ± 0.0014
x_1	21.106 ± 0.005	16.293 ± 0.009	y_1	0.2915 ± 0.0006
$\mathrm{Nu}_{t1\mathrm{prec}}$	3.6×10^{-4}	5.4×10^{-4}	$\mathrm{Nu}_{t1\mathrm{prec}}$	5.5×10^{-4}
Nu_{t2}	0.60645 ± 0.00030	3.3041 ± 0.0018	Nu_{t3}	3.3780 ± 0.0016
x_2	28.080 ± 0.006	18.963 ± 0.007	y_3	3.9032 ± 0.0004
$\mathrm{Nu}_{t2\mathrm{prec}}$	4.9×10^{-4}	5.4×10^{-4}	$\mathrm{Nu}_{t3\mathrm{prec}}$	4.7×10^{-4}
Nu_{b1}	3.48657 ± 0.00007	0.6830 ± 0.0003	Nu_{b1}	3.3077 ± 0.0018
x_1	24.993 ± 0.005	11.418 ± 0.004	y_1	1.0422 ± 0.0001
$\mathrm{Nu}_{b1\mathrm{prec}}$	2.0×10^{-5}	4.4×10^{-4}	$\mathrm{Nu}_{b1\mathrm{prec}}$	5.4×10^{-4}
Nu_{b2}	3.38959 ± 0.00014	0.7535 ± 0.0003	Nu_{b3}	0.6609 ± 0.0003
x_2	29.164 ± 0.002	30.14 ± 0.04	y_3	3.9106 ± 0.0002
$\mathrm{Nu}_{b2\mathrm{prec}}$	4.1×10^{-5}	4.0×10^{-4}	$\mathrm{Nu}_{b3\mathrm{prec}}$	4.5×10^{-4}

that, for each grid, the momentum flux Φ_u vanishes on the inlet surface S_i. Furthermore, due to the symmetry conditions and our choice of boundary conditions, several other flux components are equal to zero. These are indicated in Table 5.

We computed the fluxes defined in Table 5 on each grid, then extrapolated these values by RE. The criteria introduced in section 4.2 to define the reference values and the tolerance margins are also used here for the heat and momentum fluxes. The ranges of the extrapolation coefficient $\tilde{\alpha}$ kept to choose the extrapolated values used to define the references are $1\leq\tilde{\alpha}\leq2.5$ for the FD1 and FV3 solutions and $1\leq\tilde{\alpha}\leq3.4$ for the FE2 and FE4 solutions. The reference values with their tolerance margin are given in Table 6. The methodology used allows us to estimate the fluxes on the different surfaces with two to five significant digits, depending on the magnitude of the fluxes. More details on the methodology, the whole extrapolated

Table 5. Definition of the heat and momentum fluxes through the channel faces

	Φ_θ	Φ_u	Φ_v	Φ_w
S_i	$\int_{S_i}\left(-\frac{\partial\theta}{\partial x}+\mathrm{RePr}\,u\theta\right)dS$	$\int_{S_i}\left(p-\frac{2}{\mathrm{Re}}\frac{\partial u}{\partial x}+u^2\right)dS=0$	$\int_{S_i}\left[\frac{-1}{\mathrm{Re}}\left(\frac{\partial v}{\partial x}+\frac{\partial u}{\partial y}\right)+uv\right]dS$	$\int_{S_i}\left[\frac{-1}{\mathrm{Re}}\left(\frac{\partial w}{\partial x}+\frac{\partial u}{\partial z}\right)+uw\right]dS$
S_o	$\int_{S_o}\left(\frac{\partial\theta}{\partial x}-\mathrm{RePr}\,u\theta\right)dS$	$\int_{S_o}\left(-p+\frac{2}{\mathrm{Re}}\frac{\partial u}{\partial x}-u^2\right)\,dS$	$\int_{S_o}\left[\frac{1}{\mathrm{Re}}\left(\frac{\partial v}{\partial x}+\frac{\partial u}{\partial y}\right)-uv\right]dS$	$\int_{S_o}\left[\frac{1}{Re}\left(\frac{\partial w}{\partial x}+\frac{\partial u}{\partial z}\right)-uw\right]dS$
S_f	$\int_{S_f}-\frac{\partial\theta}{\partial y}\,dS=0$	$\int_{S_f}\frac{-1}{\mathrm{Re}}\frac{\partial u}{\partial y}\,dS$	$\int_{S_f}\left(p-\frac{2}{\mathrm{Re}}\frac{\partial v}{\partial y}\right)dS$	$\int_{S_f}\frac{-1}{\mathrm{Re}}\frac{\partial w}{\partial y}\,dS$
S_s	$\int_{S_s}\frac{\partial\theta}{\partial y}\,dS=0$	$\int_{S_s}\frac{1}{\mathrm{Re}}\frac{\partial u}{\partial y}\,dS=0$	$\int_{S_s}\left(-p+\frac{2}{\mathrm{Re}}\frac{\partial v}{\partial y}\right)dS$	$\int_{S_s}\frac{1}{\mathrm{Re}}\frac{\partial w}{\partial y}\,dS=0$
S_b	$\int_{S_b}-\frac{\partial\theta}{\partial z}\,dS$	$\int_{S_b}\frac{-1}{\mathrm{Re}}\frac{\partial u}{\partial z}\,dS$	$\int_{S_b}\frac{-1}{\mathrm{Re}}\frac{\partial v}{\partial z}\,dS$	$\int_{S_b}\left(p-\frac{2}{\mathrm{Re}}\frac{\partial w}{\partial z}\right)dS$
S_t	$\int_{S_t}\frac{\partial\theta}{\partial z}\,dS$	$\int_{S_t}\frac{1}{\mathrm{Re}}\frac{\partial u}{\partial z}\,dS$	$\int_{S_t}\frac{1}{\mathrm{Re}}\frac{\partial v}{\partial z}\,dS$	$\int_{S_t}\left(-p+\frac{2}{\mathrm{Re}}\frac{\partial w}{\partial z}\right)dS$
S_{tot}	0	0	0	$\int_{\Omega/2}\frac{-\mathrm{Ra}}{\mathrm{Re}^2\mathrm{Pr}}\theta\,dV=I_{\mathrm{buo}}$

Table 6. Reference values of the heat and momentum fluxes through channel surfaces and buoyancy term integral. The values 0.0 correspond to the theoretical values given in Table 5

	Φ_θ	Φ_u	Φ_v	Φ_w
S_i	$-(1.021 \pm 0.010) \times 10^{-8}$	0.0	$-(2.1354 \pm 0.0010) \times 10^{-2}$	$(7.00 \pm 0.07) \times 10^{-5}$
S_o	-87.630 ± 0.003	72.1704 ± 0.0008	$(3.07 \pm 0.05) \times 10^{-2}$	$(1.670 \pm 0.013) \times 10^{-2}$
S_f	0.0	-3.984 ± 0.004	-409.35 ± 0.04	-1.7678 ± 0.0006
S_s	0.0	0.0	409.31 ± 0.01	0.0
S_b	479.97 ± 0.05	-35.416 ± 0.013	2.6366 ± 0.0008	-2249.64 ± 0.04
S_t	-392.31 ± 0.08	-32.786 ± 0.008	-2.5868 ± 0.0004	1930.967 ± 0.015
S_{tot}	0.0	0.0	0.0	-320.444 ± 0.014
I_{buo}				-320.431 ± 0.007

values of each contributor, the values on the finest grids, and the $\tilde{\alpha}$ values can be found in [33].

6. CONCLUSIONS

A reference solution of a first numerical benchmark for a steady three-dimensional mixed-convection flow in a horizontal rectangular channel, partially heated from below and cooled from above, has been presented. The methodology used to establish this solution is based on the use of four different numerical methods (second-order FD and FV methods, and third-order FE methods), Richardson extrapolations (RE) on very fine grids, and cubic spline interpolations. The reference values are proposed for the dynamical and thermal fields, in the form of local, integral or differential quantities such as local extrema of the primitive variables and Nusselt numbers, surface heat and momentum fluxes, volume integrals of the temperature, and kinetic energy and pressure loss. These reference solutions are generally given up to four or five significant figures. The numerical values of all the reference quantities are presented in tables with their accuracy margins. Streamwise and spanwise profiles of the velocity components, temperature, and Nusselt numbers are also provided.

The difficulty in the establishment of the reference solution of the present benchmark problem is that a discontinuity takes place in the thermal gradient over the horizontal plates at $x = 0$, which not only significantly restricts the conditions of application of RE to establish reference solutions, but also complicates its analysis. That is why the consequences of this discontinuity on RE and on the establishment of a reference solution of the benchmark problem are discussed separately in a more theoretical article [15]. Furthermore, a comprehensive and detailed technical report of this benchmark problem, with other reference values, is available online [33].

REFERENCES

1. X. Nicolas, A. Benzaoui, and S. Xin, Numerical Simulation of Thermoconvective Flows and More Uniform Depositions in a Cold Wall Rectangular APCVD Reactor, *J. Crystal Growth*, vol. 310, pp. 174–186, 2008.

2. Q. H. Wang and Y. Jaluria, Instability and Heat Transfer in Mixed-Convection Flow in a Horizontal Duct with Discrete Heat Sources, *Numer. Heat Transfer A*, vol. 42, pp. 445–463, 2002.
3. X. Nicolas, Bibliographical Review on the Poiseuille-Rayleigh-Bénard Flows: The Mixed Convection Flows in Horizontal Rectangular Ducts Heated from Below, *Int. J. Thermal Sci.*, vol. 41, pp. 961–1016, 2002.
4. H. Ben Hamed, R. Bennacer, T. Langlet, H. Sammouda, and H. Béji, Numerical 3D-Study of Poiseuille Rayleigh Benard Soret Problem in a Finite Extent Paralellepipedic Duct, *Numer. Heat Transfert A*, vol. 55, pp. 534–552, 2009.
5. O. Rahli, R. Bennacer, K. Bouhadef, and D. E. Ameziani, Three-Dimensional Mixed Convection Heat and Mass Transfer in a Rectangular Duct: Case of Longitudinal Rolls, *Numer. Heat Transfer A*, vol. 59, pp. 349–371, 2011.
6. K. C. Chiu and F. Rosenberger, Mixed Convection between Horizontal Plates—1: Entrance Effects, *Int. J. Heat Mass Transfer*, vol. 30, pp. 1645–1654, 1987.
7. M. T. Ouazzani, J. K. Platten, and A. Mojtabi, Etude Expérimentale de la Convection Mixte Entre Deux Plans Horizontaux à Températures Différentes—2, *Int. J. Heat Mass Transfer*, vol. 33, pp. 1417–1427, 1990.
8. A. Benzaoui, X. Nicolas, and S. Xin, Efficient Vectorized Finite Difference Method to Solve the Incompressible Navier-Stokes Equations for 3D Mixed Convection Flows in High Aspect Ratio Channels, *Numer. Heat Transfer B*, vol. 48, pp. 277–302, 2005.
9. M. Medale and X. Nicolas, CALL FOR CONTRIBUTIONS: Towards Numerical Benchmark Solutions for 3D Mixed Convection Flows in Rectangular Channels Heated from Below, *Int. J. Thermal Sci.*, vol. 45, pp. 331–333, 2006.
10. K. F. Alvin, W. L. Oberkampf, B. M. Rutherford, and K. V. Diegert, Methodology for Characterizing Modeling and Discretization Uncertainties in Computational Simulation (read §4, pp. 28–37), SAND2000-0515, Sandia Natl. Labor., Albuquerque, NM, 2000.
11. P. J. Roache, Perspective: A Method for Uniform Reporting of Grid Refinement Studies, *J. Fluids Eng.*, vol. 116, pp. 405–413, 1994.
12. W. L. Oberkampf and T. Trucano, Verification, and Validation in Computational Fluid Dynamics (read §3.3, pp. 31–42), SAND2002-0529, Sandia Natl. Labor., Albuquerque, NM, 2002, also in Prog. Aerospace Sci., vol. 38, pp. 209–272, 2002.
13. C. J. Roy, Review of Code and Solution Verification Procedures for Computational Simulation, *J. Comput. Phys.*, vol. 205, pp. 131–156, 2005.
14. H. Pabiou, S. Mergui, and C. Bénard, Wavy Secondary Instability of Longitudinal Rolls in Rayleigh–Bénard–Poiseuille Flows, *J. Fluid Mech.*, vol. 542, pp. 175–194, 2005.
15. X. Nicolas, S. Gounand, M. Medale, and S. Glockner, Benchmark Solution for a Three-Dimensional Mixed Convection Flow - Part 2: Analysis of Richardson Extrapolation in the Presence of a Singularity, *Numer. Heat Transfer B*, vol. 60, pp. 346–369, 2011.
16. X. Nicolas, J. M. Luijkx, and J. K. Platten, Linear Stability of Mixed Convection Flows in Horizontal Rectangular Channels of Finite Transversal Extension Heated from below, *Int. J. Heat Mass Transfer*, vol. 43, pp. 589–610, 2000.
17. K. Goda, A Multistep Technique with Implicit Difference Schemes for Calculating Two- or Three-Dimensional Cavity Flows, *J. Comput. Phys.*, vol. 30, pp. 76–95, 1979.
18. J. L. Guermond and J. Shen, A New Class of Truly Consistent Splitting Schemes for Incompressible Flows, *J. Comput. Phys.*, vol. 192, pp. 262–276, 2003.
19. S. A. Orszag, M. Israeli, and M. O. Deville, Boundary Conditions for Incompressible Flows, *J. Sci. Comput.*, vol. 1, pp. 75–111, 1986.
20. G. E. M. Karniadakis, M. Israeli, and S. A. Orszag, High-Order Splitting Methods for the Incompressible Navier-Stokes Equations, *J. Comput. Phys.*, vol. 97, pp. 414–443, 1991.

21. T. C. Papanastasiou, N. Malamataris, and K. Ellwood, A New Outflow Boundary Condition, *Int. J. Numer. Meth. Fluids*, vol. 14, pp. 587–608, 1992.
22. S. Balay, K. Buschelman, W. D. Gropp, D. Kaushik, M. G. Knepley, L. Curfman McInnes, B. F. Smith, and H. Zhang, Petsc Web pages, www.mcs.anl.gov/petsc, 2007.
23. L. J. P. Timmermans, P. D. Minev, and F. N. Van De Vosse, An Approximate Projection Scheme for Incompressible Flow Using Spectral Elements, *Int. J. Numer. Meth. Fluids*, vol. 22, pp. 673–688, 1996.
24. B. P. Leonard, A Stable and Accurate Convection Modelling Procedure Based on Quadratic Upstream Interpolation, *Comput. Meth. Appl. Mech. Eng.*, vol. 19, pp. 59–98, 1979.
25. E. Ahusborde and S. Glockner, A 2D Block-Structured Mesh Partitioner for Accurate Flow Simulations on Non-Rectangular Geometries, *Comput. Fluids*, vol. 43, pp. 2–13, 2011.
26. R. D. Falgout, J. E. Jones, and U. M. Yang, The Design and Implementation of Hypre, a Library of Parallel High Performance Preconditioners, in A. M. Bruaset and A. Tveito, (eds.), *Numerical Solution of Partial Differential Equations on Parallel Computers*, Springer-Verlag, UCRL-JRNL-205459, vol. 51, pp. 267–294, 2006.
27. A. Ern and J. L. Guermond, *Theory and Practice of Finite Elements*, Applied Mathematical Series, vol. 159, chap. 4, Springer-Verlag, New-York, 2004.
28. S. Turek, *Efficient Solvers for Incompressible Flow Problems—An Algorithmic and Computational Approach*, Lecture Notes in Computational Science and Engineering, vol. 6, chap. 3, Springer-Verlag, Berlin, 1999.
29. A. Quarteroni, F. Saleri, and A. Veneziani, Factorization Methods for the Numerical Approximation of Navier-Stokes Equations, *CNAME*, vol. 188, pp. 505–526, 2000.
30. Y. Saad, *Iterative Methods for Sparse Linear Systems*, 2d ed., chaps. 8 and 10, SIAM, Philadelphia, 2003.
31. Y. Notay, An Aggregation-Based Algebraic Multigrid Method, *Electron. Trans. Numer. Anal.*, vol. 37, pp. 123–146, 2010.
32. Cast3m website, www-cast3m.cea.fr.
33. X. Nicolas, M. Medale, S. Gounand, and S. Glockner, Benchmark Solution for a Three-Dimensional Mixed Convection Flow—Detailed Technical Report, www.sft.asso.fr/Local/sft/dir/user-3775/documents/DocumentsDivers/SFT_Report_benchmark_PRB_2011.pdf, pp. 1–44, 2011.

APPENDIX

The analytical solution of the dimensionless Poiseuille profile is equal to $u_{\text{Pois}}(y,z) = U_{\text{Pois}}(y,z)/U_{\text{mean}}$, where the dimensional Poiseuille profile $U_{\text{Pois}}(y, z)$ is given by [16]

$$\frac{U_{\text{Pois}}(y,z)}{U^{\circ}} = 6z(1-z) + \frac{48}{\pi^3}\sum_{n=0}^{\infty}\frac{(-1)^{n+1}\cosh[(2n+1)\pi(y-B/2)]\cos[(2n+1)\pi(z-1/2)]}{(2n+1)^3\cosh[(2n+1)\pi B/2]} \tag{10}$$

where $U^{\circ} = \left(-H^2/12\mu\right)(\partial P/\partial X)$ is the average velocity of the "two-dimensional" Poiseuille flow, i.e., in a two-dimensional channel or between two infinite plates, and where the dimensional average velocity U_{mean} of the Poiseuille flow is given by

$$\frac{U_{\text{mean}}}{U^{\circ}} = 1 + \frac{192}{\pi^5} \sum_{n=0}^{\infty} \frac{(-1)^{n+1} \sinh[(2n+1)\pi B/2] \sin[(2n+1)\pi/2]}{(2n+1)^5 B \cosh[(2n+1)\pi B/2]} \tag{11}$$

Thus the inlet dimensionless Poiseuille profile $u_{\text{Pois}}(y, z)$ is given by the ratio of Eqs. (10) and (11), where about 25 terms are kept in the series to obtain a sufficiently accurate entrance velocity profile. Note that in (10) and (11), the hyperbolic cosine at the denominator diverges when n is high. To avoid any problem, the two hyperbolic cosines of the series can be transformed in real exponentials via the Euler relations. Thus, by denoting $N = 2n + 1$, the ratio of the two hyperbolic cosines writes as

$$\frac{\cosh[N\pi(y - B/2)]}{\cosh[N\pi B/2]} = \exp[N\pi(y - B)] \frac{1 + exp[-2N\pi(y - B/2)]}{1 + \exp(-N\pi B)} \tag{12}$$

To avoid the divergence of $\exp[-2N\pi(y - B/2]$ when N is high, the Poiseuille profile must only be computed for $(B/2) \leq y \leq B$. The symmetry with respect to the median vertical plane is used to compute the Poiseuille profile for $0 \leq y \leq B/2$.